

## Turbulence statistics and distribution of turbulent eddies for jet flow and rigid surface interaction

S. ROY, K. DEBNATH<sup>1)</sup>, B. S. MAZUMDER

*Fluid Mechanics and Hydraulic Laboratory (FMHL)  
Department of Aerospace Engineering and Applied Mechanics  
Indian Institute of Engineering Science and Technology (IEST)  
Shibpur 711103, India  
email<sup>1)</sup>: debnath\_koustuv@yahoo.com*

THE BEHAVIOR OF TURBULENT EDDIES within the self-similar region of a rigid surface interacting round jet is experimentally investigated. Results show that the turbulent jet flow structure is significantly affected due to the rigid surface interaction; particularly within the lower portion of the jet shear layer. It is observed that the jet and rigid surface interactions rather enhance the scale of axial velocity fluctuations within the intermediate region of the jet. An additional mixing layer is observed in the lower shear layer region close to the rigid surface due to the production of eddies from the rigid surface. The depth of penetration of the fluctuating eddies decreases significantly at the mixing layer region and this mixing layer acts like a shield which restricts the downward propagation of fluctuating eddies from the plane of symmetry of the jet. The results suggest that the region below the mixing layer can be treated as the shear less mixing region. The interesting consequence of this is that the rate of production of vorticity is enhanced below the mixing layer close to the rigid surface. Also, the enstrophy destruction is favored over enstrophy production at the upper portion of the mixing layer, and exactly the opposite phenomenon is observed in the lower portion of the mixing layer.

**Key words:** turbulent round jet, rigid surface interaction, statistical moments, wavelet analysis, mixing layer.

Copyright © 2018 by IPPT PAN

### 1. Introduction

A LARGE REYNOLDS NUMBER FLOW DISCHARGE from a circular nozzle generally forms the turbulent round jet. As the jet issues into a quiescent background, the background fluid is entrained into the jet by engulfment and nibbling mechanisms and the jet is spread in the radial direction with downstream axial distance [1]. Also, the initial momentum is distributed very delicately and finally, the viscous action dissipates the energy leading to the breakdown of the jet [2]. Application of the turbulent jet covers a broad area in the aerospace industry. Wide applications of the turbulent jet are also observed in many diverse

engineering fields such as disposal of waste water, gaseous or pollutant release in air or water from the chemical plants, dispersion of pollutants in the atmosphere, the propeller jet flows impinging from river traffics, estuarine flows and volcanic ash clouds. Due to the wide range of applications of the turbulent jets, the dynamics of the jet flow field have been extensively studied during last few decades [1, 3–6]. WYGNANSKI and FIEDLER [7] performed some measurements in the self-similar region of a jet to study the intermittent fluctuations. HUSSEIN *et al.* [3] studied the axisymmetric turbulent flow of a top-hat jet profile to investigate the higher order moments using hot-wire and burst-mode LDA techniques for jet Reynolds number  $10^5$ . They used the velocity data to compute the energy balance for the jet flow, and also to estimate the pressure-velocity and pressure-strain rate correlations, which agreed well with the equations of motion. Furthermore, modern aircraft concepts incorporate over-the-wing engine designs that impart a shielding effect for the jet exhaust noise, and an interaction between the jet and flat rigid surface occurs. In some of the arrangements, the jet exhaust is made to pass through a duct before being released as a free jet wherein interaction of jet with the flat rigid surface is pertinent. For the improved design of such arrangements, understanding the physics of jet surface interaction is of the utmost importance. Understanding the physics of the turbulent flow structure within the jet for jet surface interaction is also an important subject for the design of the surface cover of the nozzle exit. Using experimental data CHASE [8] developed a model for the hydrodynamic pressure and spectra.

Noise generation due to the jet-surface interaction was examined by several investigators [9–11]. An experimental study was carried out on the interaction of a rectangular jet with a rigid flat-plate by ZAMAN *et al.* [12] wherein a surprising resonant interaction between the jet and the rigid surface was observed. WANG *et al.* [13] studied the mixing characteristics of two submerged parallel jets issuing from two rectangular channels. They also studied the scale and the development time of different-size eddies in the mixing region using continuous wavelet transform. In the past wavelet transform was used to analyze the time varying signals in different fields of science and engineering [14–17]. PANIZZO *et al.* [18] used the wavelet analysis to observe the records of water level surface. They noticed that this method is capable of providing information on the distribution of wave energy in the time and frequency domains. FARGE [39] evaluated some basic requirements for the selection of a proper wavelet function, for instance, the admissibility condition. PANDRES [41] stated that admissibility conditions for wave functions are obtained from general quantum-mechanical principles. It may be helpful for measurement of the position of a particle (a physical approach). Further it must have zero mean and be contained in both time and frequency domains.

CAMUSSI and GUJ [42] computed the orthogonal wavelet decomposition in combination with the form of scaling named extended self-similarity in jet turbulence. The longitudinal velocity component seems to be affected by the passage of vortex rings belonging to the mixing layer region. Such large structures induce intermittency even at the smallest scales. Further, CAMUSSI and GUJ [43] performed an analysis of coherent structures characterized by random phase using wavelet decomposition within the near field of a high Reynolds number turbulent jet flow based on experimental data. GRIZZI and CAMUSSI [44] examined the wavelet analysis of the pressure field generated by a subsonic, single stream, round jet. Also, it is more useful for the study of non-stationary water waves. Recently ROY *et al.* [19] have reviewed its application on velocity time series data for the quantification of distribution of eddy scales for the wave current combined flow.

MARCO *et al.* [36] stated that as the axial velocity values depend both on the axial position and the flat plate distance from the orifice exit, also the spectral density of pressure fluctuations is affected due to the presence of a flat plate. Recently, DE ALMEIDA [37] have studied the characterization of velocity and acoustic fields from a single-stream free jet and showed some measurement technique by a triple sensor hot-film anemometer. The outcomes from these studies depicts that the pressure field around a jet is affected due to the presence of a flat rigid surface. The ambient fluid entrainment from the immediate surroundings into a free turbulent jet may act as a catalyst in formation of a sleeve of low pressure around the jet. This sleeve of low pressure exerts a force on the jet in the radial direction which is equal in all directions for a free jet. Thus, the jet axis is aligned along a straight line. However, if a solid surface is placed close, and approximately parallel to the jet, the entrainment of fluid from between the solid surface and the jet causes a reduction in fluid pressure on that side of the jet (in the present case a bottom shear layer). However, the pressure on the upper shear layer remains unchanged. This pressure difference between the lower and upper sides of the jet possibly deviates the jet flow field towards the nearby surface. This phenomenon is known as the Coandă effect [38]. This Coandă effect induced forces which can cause lift and other forms of motion, depending on the orientation of the jet and the surface.

However, in spite of all the aforementioned investigations on the turbulent free jet and turbulent jet-surface interaction flows, no attempt has been made to investigate the turbulence statistics and the behavior of coherent flow structures in and around the turbulent jet impinging on the quiescent background parallel to a flat rigid surface. The present study aims at understanding the turbulence, statistical moments of velocity fluctuations, turbulent mixing length, turbulent kinetic energy (TKE) flux, and the distributions of eddy scales in the time and frequency domains at the self-similar region of the turbulent round jet

flow interacting with a flat rigid surface parallel to the jet flow direction. More precisely, an attempt is being made on understanding how the components of TKE flux, TKE, energy dissipation, turbulent length scale, velocity-derivative skewness and enstrophy-production vary within the self-similar region near the flat surface. It is expected that the present study has the potential to be useful to the worldwide spectrum of scientists and engineers representing fields of interest from environmental flows to jet flows in aerospace applications.

## 2. Experimental setup

### 2.1. Test channel

Experiments were performed in a water tank at the Fluid Mechanics and Hydraulic Laboratory (FMHL), Indian Institute of Engineering Science and Technology (IIST), Shibpur, India. The water tank used in the present experiments, shown in Fig. 1, is 6 m in length, 0.9 m wide and 0.9 m of depth. The front and rear gate were adjusted to maintain the desired flow depth ( $h$ ) at a particular jet discharge. The depth was continuously monitored during the experiment against graduated scales attached to the perspex wall of the test section. The flow was made to pass over the front and rear gate to release the excess water (issued from jet flow) to ensure the uniform flow depth.

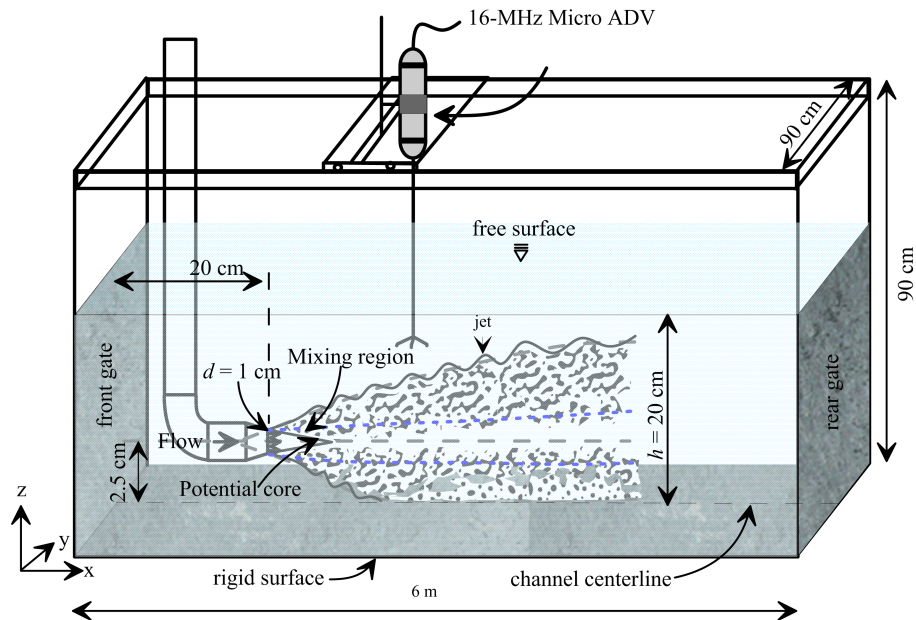


FIG. 1. Schematic diagram of the test section.

## 2.2. Jet apparatus

A turbulent round jet impinged on a quiescent background at the centerline of the water tank positioned at 20 cm distance from the front gate and 2.5 cm height above the bottom surface (Fig. 1). LAUNDER and RODI [35] noted that the Reynolds stress field generated from the wall may play a significant role in the generation of streamwise vorticity for wall turbulence when the ratio of transverse and vertical jet half width is less than 2:1 (at the fully developed region). It may be noted here that the present experiments were conducted with all the cases where the ratio of transverse and vertical jet half width was less than 2:1. Thus the present experimental cases fall under the wall jet category. The vertical location of the orifice was fixed at a particular level, since the variation of the orifice distance from the boundary was not the aim of the present study.

The water was supplied from a reservoir tank kept at a height of 2.55 m above the tank bed. A constant head of water in the tank was maintained for a particular jet case to achieve constant jet discharge. The jet discharge was controlled by the discharge control gate valve. The jet was issued from the constant head reservoir tank via Poly Vinyl Chloride (PVC) pipe of 2.5 cm diameter, and the orifice diameter was 1 cm. In order to join the 1 cm orifice diameter tube with the 2.5 cm diameter pipe, a 2.5 cm to 1 cm reducer was used after the discharge control gate valve. One 85 cm long vertical L-shaped bend tube with the circular orifice of 1 cm diameter was used to release the jet horizontally parallel to the bottom surface. Note that the center of the jet orifice was kept at a distance of 20 cm downstream of the front gate and 2.5 cm above the bottom surface level to achieve the surface interacting turbulent round jet (Fig. 1).

## 3. Jet flow measurements

In order to measure the instantaneous velocity components, a three-dimensional acoustic Doppler velocimeter (ADV) was used for this particular experiment. The sampling volume was located 5 cm below the ADV probe to reduce flow interference by the probe. The ADV operated by measuring acoustic signals reflected off particles in the flow, and therefore SNR should be maximum to get good data quality. In order to increase the SNR of the ADV, some neutrally buoyant very fine particles were added to water. The minimum SNR and correlation parameters specified by the manufacturer are 15 dB and 70%, respectively. In order to receive good quality of data, the SNR and correlation parameter ranges were maintained at  $> 20$  dB and correlation  $> 90\%$  throughout the experiment.

The jet flow measurements were performed for the jet released into the quiescent background with jet Reynolds numbers  $Re_j(u_j d \nu) = 8000, 15000,$  and  $22000$ , where  $u_j$  is the orifice exit flow velocity,  $\nu$  is the kinematic viscosity and

$d$  is the diameter of the orifice. To perform the experiment, the round jet was issued at the test tank centerline and the jet was kept parallel to the bottom surface. After a certain time, velocity data were collected using ADV at a sampling rate of 40 Hz for 3 minutes from each of eight different locations along the center line of the test water tank starting from the jet orifice towards the downstream direction. The normalized distance of locations, considering the center of orifice as reference, were  $x/d = 5, 10, 20, 30, 40, 50, 60$ , where  $x$  is the axial downstream distance from the center of the jet orifice ( $x/d = 0$ ).

#### 4. Data analysis

In turbulent jet flow the instantaneous streamwise ( $u$ ), horizontal ( $v$ ), and vertical ( $w$ ) velocity components in the  $(x, y, z)$  directions are decomposed into a mean part and fluctuating part as

$$(4.1) \quad u = u_{(x)} + u'_{(x)}, \quad v = v_{(y)} + v'_{(y)}, \quad w = w_{(z)} + w'_{(z)},$$

where  $u_{(x)}, v_{(y)}, w_{(z)}$  are the time-averaged velocity components and  $u'_{(x)}, v'_{(y)}, w'_{(z)}$  are the corresponding velocity fluctuations. The time-averaged velocity components  $u_{(x)}, v_{(y)}, w_{(z)}$  are given as:

$$(4.2) \quad u_{(x)} = \frac{1}{n} \sum_{i=1}^n u_i, \quad v_{(y)} = \frac{1}{n} \sum_{i=1}^n v_i, \quad w_{(z)} = \frac{1}{n} \sum_{i=1}^n w_i.$$

Streamwise rms velocity ( $u_{rms}$ ) is computed by the method defined as:

$$(4.3) \quad u_{rms} = \sqrt{\overline{u'^2_{(x)}}} = \sqrt{\frac{1}{n} \sum_{i=1}^n ((u)_i - u_{(x)})^2}.$$

The time-averaged Reynolds shear stress component ( $u, w$ ) are defined as:

$$(4.4) \quad \tau_{(uw)} = -\overline{\rho u'_{(x)} w'_{(z)}} = -\frac{\rho}{n} \sum_{i=1}^n (u_i - u_{(x)})(w_i - w_{(z)}).$$

An estimation of the uncertainty for statistical turbulence parameters is necessary for having information on the data quality pertaining to statistical errors arising due to the physical constraint of the measurement technique used by the instrument as well as uncertainties associated with the boundary conditions.

The estimates of the variance errors of the sample mean and variance for uncorrelated samples applicable for any statistical parameter distribution can

be defined as [45]:

$$(4.6) \quad \zeta_{\text{mean}} = \frac{\zeta_u}{N_{\text{mef}}}$$

$$(4.7) \quad \zeta_{\text{var}} = \frac{2}{N_{\text{vef}}}(\zeta_u^2),$$

where  $\zeta_u$  represents the sample variance of the variable  $u$ .

$$(4.7) \quad N_{\text{mef}} = \frac{T_t}{2T_s},$$

$$(4.8) \quad N_{\text{vef}} = \frac{T_t}{T_s},$$

where  $T_t$  is the total sampling time and  $T_s$  is the integral time scale using the autocorrelation method.

The moving block bootstrap (MBB) technique [46] is a conventional tool for quantification of the uncertainty with 95% confidence intervals for each turbulence parameter and is used herein for uncertainty analysis. An essential parameter in the MBB technique is the optimum length of the block. POLITIS and WHITE [47] and GARCÍA *et al.* [45] reported that the optimum block length can be estimated based on the observed autocorrelation function of each recorded signal. In this present study, the optimum block length is estimated using the method proposed in [47] and [46]. The synthetic data set was computed using the MBB method for a wide range of flow conditions ( $5 \times 10^3 \leq Re \leq 25 \times 10^3$ ). The velocity signal in each coordinate direction was synthesized with 1000 replications, each of 3 minutes time duration with data intervals at 40 Hz frequency. Here as a sample case we show the data computed at a distance  $x/d = 30$  from the orifice exit in a particular point  $z/h = 0.12$ .

Figures 2a and 2b show the error variance of the sample mean and variance, respectively. These parameters were computed for each signal based on the MBB technique and the values are plotted as a function of the values obtained from experimental data using Eqs. (4.5) and (4.6). It may be noted that the average relative error of the standard error of the sample mean is approximately 3.8%. For the sample variance, the average relative error is obtained as 15.1%. Figures 2a and 2b reveal a good agreement between the signal synthesized by the MBB technique and that computed from Eqs. (4.5) and (4.6).

Figures 2c and 2d show the comparison plots between probability distribution of the  $T_s$  and  $u_{\text{mean}}$  computed from the experimental data and using MBB technique. The error values for both the parameters as shown in Figs. 2c and 2d are  $\leq 14.5\%$ .

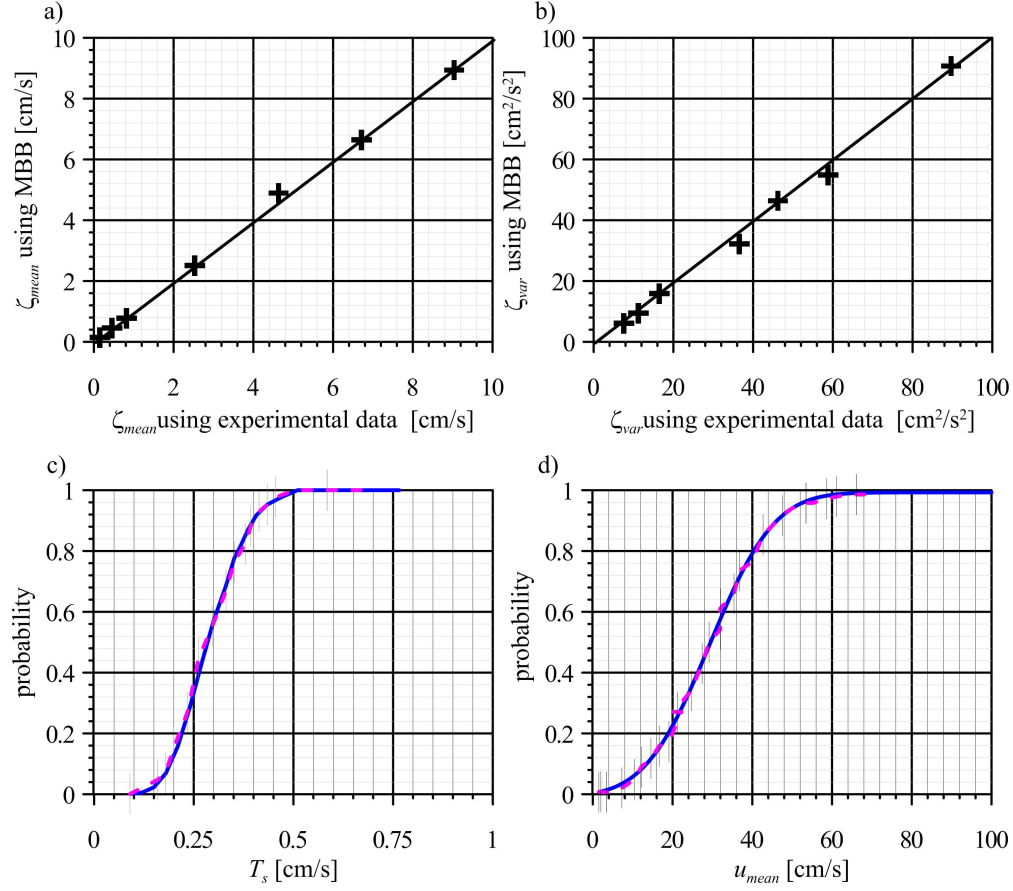


FIG. 2. Plots of uncertainty analysis. a) Comparison between standard errors of the sample mean calculated for each synthetic signal using MBB technique and Eq. (4.5), the continuous line represents well conformity between the two selections. b) Comparison between standard errors of the sample variance calculated for synthetic signal using MBB technique and Eq. (4.6), the continuous line represents the perfect agreement between the two selections. c) Comparison between probability distribution of the integral time scale  $T_s$  estimated from the experimental data (dotted line) and using MBB technique (continuous line). d) Comparison between probability distribution of the sample mean estimated from the experimental data (dotted line) and using MBB technique (continuous line).

## 5. Validation of turbulent flow

The profiles of the axial mean velocity  $u_{(x)}$  against the radial distance  $r$  for an axisymmetric turbulent free jet of  $Re_j = 22000$  issuing into a quiescent background at  $(x/d = 30)$  are plotted in Fig. 3a. The turbulent free jet issued into the quiescent background at a vertical distance of 10 cm above the bottom surface. It was ensured that the jet is free from any boundary interactions (such

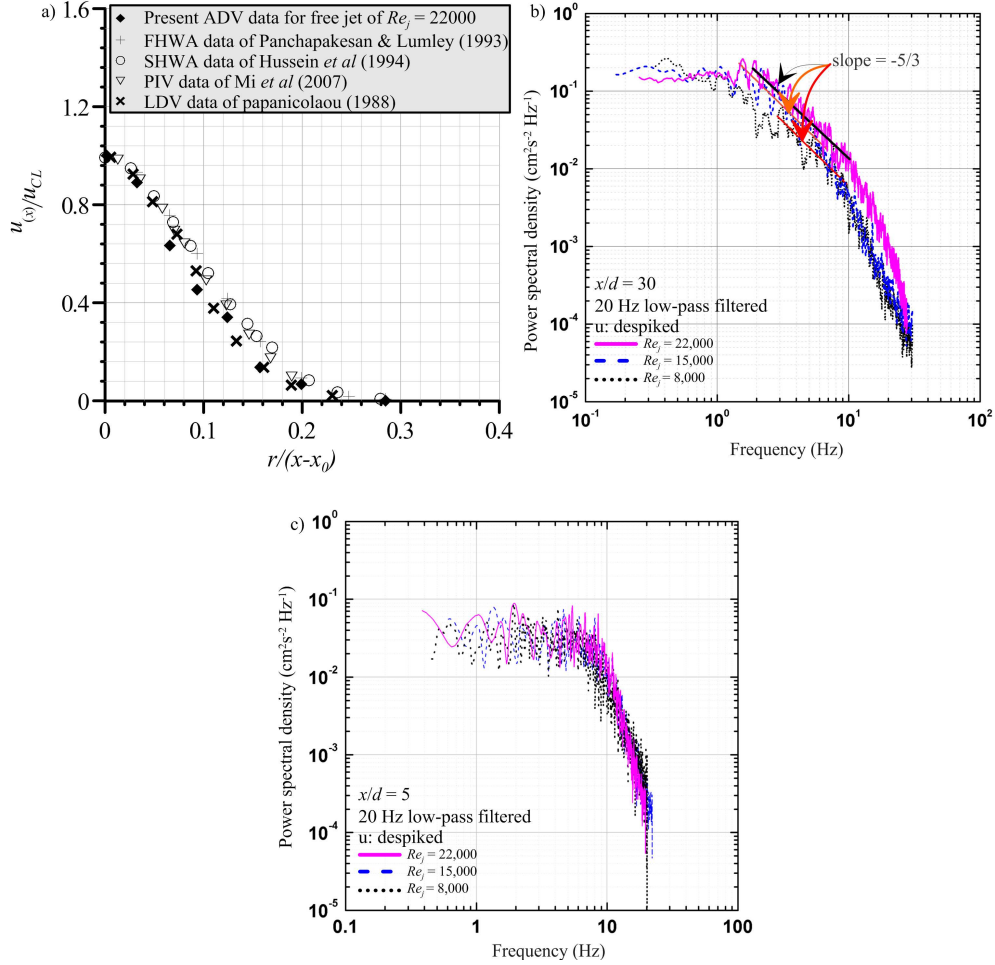


FIG. 3. a) Transverse profiles of the axial jet velocity (free jet). b) Power spectral density (PSD) of free jet axial velocity issuing into the quiescent background for all three jet Reynolds numbers at the location  $x/d = 30$ . c) PSD for free jets at  $x/d = 5$ .

as side wall interaction, a bottom surface, and free surface interaction). Here the axial mean velocity  $u(x)$  and the radial distance  $r$  are normalized by the centerline velocity  $u_{CL}$  and  $(x - x_0)$  respectively, here  $x_0$  signifies the virtual origin. The radial profiles of the axial mean velocity for the case of the present dataset agree well with those of existing results, which substantiate the present velocity data.

The power spectral density serves as a test to ensure the accuracy of the measurement of velocity data [20]. The velocity data were collected by using ADV for three different jet Reynolds numbers  $Re_j = 8000, 15000, 22000$ , at

$x/d = 30$  in the centerline of the jet. In the estimation of the power spectral densities, the velocity data were de-spiked and made to pass through the low-pass filter with cut-off frequency 20 Hz; and plotted against frequency in log-log scale for the axial velocity (Fig. 3b). A clear  $-5/3$  slope at the inertial sub-range is observed in Fig. 3b for all three Reynolds number cases, which ensures the reliability of measurement for the jet flow released into the quiescent background without surface interaction (similar to POPE [20]).

WINANT and BROWAND [33] showed the results of the initial nonlinear growth of the turbulent free jet and stated that a row of vortical structures containing most of the vorticity are initially distributed in the steady shear layer (near the orifice exit). Further, the perturbations in the boundaries of the constant vorticity region are exposed to and influenced by the vertical and radial velocities which cause the perturbations to grow. Moreover, the vorticity-containing region becomes periodically fatter and thinner, and the vortical areas are cramped within narrow boundaries. Finally, the vorticity is shown as discrete lumps. The pairing process results from the mutual interaction of neighbouring vortices. It is clear from Fig. 3b that the vortex (nonlinear oscillations of turbulent eddies) frequencies are  $f = 0.3$  Hz, 1 Hz, 1.5 Hz for  $Re_j = 8000$ , 15000, 22000 at the center line of the jet at  $x/d = 30$ ; and the corresponding jet Strouhal number  $S_h = fd/u$  are 0.0037, 0.006 and 0.0068, respectively. However,  $f = 0.7$  Hz, 1.4 Hz and 2.3 Hz are observed for  $Re_j = 8000$ , 15000 and 22000 (Fig. 3c); and the corresponding  $S_h = 0.0087$ , 0.0093 and 0.01, respectively at the center line of the jet for  $x/d = 5$  (initial region of the jet, Fig. 3c). These results depict that the row of vortical structures that are contained in the steady shear layer are distributed at a higher frequency, at the initial region of the jet ( $x/d = 5$ ) compared to that of at  $x/d = 30$ . Thus a higher Strouhal number at  $x/d = 5$  is observed compared to that at  $x/d = 30$ . It may be possibly due to the pairing process, which occurs from the mutual interaction of neighbouring vortices within the interface of shear layer and outer region at  $x/d = 30$ . These play a significant role in the distribution of the streamwise eddies at the core region of the jet. It may be noted that the present experimental results are in good agreement with ZAMAN and HUSSAIN [34].

## 6. Experimental results

### 6.1. Mean velocity distribution

Figure 4 shows the comparative study of the normalized jet flow ( $u_j/u_{CL}$ ) against the normalized distance  $x/d$  along the axial central line of the jet, where  $u_{CL}$  is the mean axial centerline velocity, which is inversely proportional to axial jet downstream distance  $x$ . The results of the present experimental data for a free

jet are in good agreements with other studies. Whereas, the axial velocity values decay at the region ranging from  $x/d \approx 10$  to 35 for jet-surface interaction cases (Fig. 4). Further, a velocity jump is observed at the location  $x/d \approx 40$  to 45. Thus it is evident that the rigid surface is efficient in modulating the velocity structure of the jet. It is evident from Fig. 4 that the mean axial velocity varies inversely with the downstream distance. The mean velocity of the jet varies within the self-similar region as:

$$(6.1) \quad u_{CL}/u_j = B/[(x - x_0)/d],$$

where  $B$  is the proportionality constant known as the decay constant and  $x_0$  is the virtual origin of the jet. RAJARATNAM [21] reported that the virtual origin  $x_0$  was situated behind the actual orifice, whereas several experiments were reported positioning the virtual origin at the leading of the orifice. In fact, the debate exists regarding its precise location, however, for the practical purposes, the virtual origin is taken at the leading edge of the orifice in many studies and is adopted herein. Similarly, the jet half-width ( $r_{1/2}$ ) is directly proportional to the downstream distance as  $r_{1/2} = S(x - x_0)$ , where  $S$  is the proportionality constant known as spreading rate constant [22]. The term half-width of the jet is defined as the radial position at which the centerline velocity falls to half of its value. For the present case, the constants  $B$  and  $S$  are estimated from the observed data using the virtual origin at  $x_0/d = 0$  similar to PANCHAPAKESAN, LUMLEY [23], while the  $x_0/d = 2.7$  used by HUSSEIN *et al.* [3]. The estimated values of  $B$  and  $S$  are compared with the existing values for validation and are

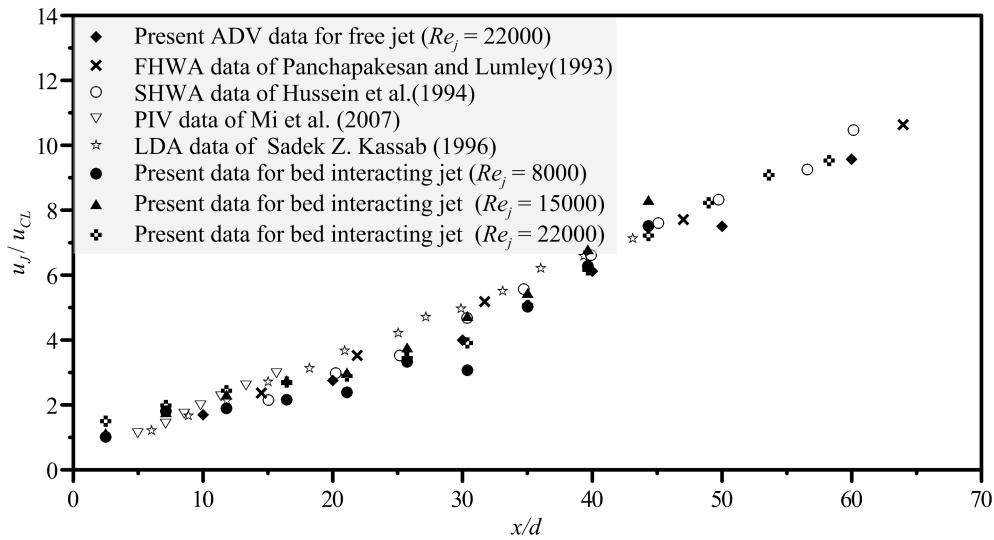


FIG. 4. The normalized jet flow velocity ( $u_j/u_{CL}$ ) against the normalized distance ( $x/d$ ).

presented in Table 1. By comparison of these values with the present data, it can be stated that the decay rate is almost similar in the self-similar region of the jet, and is almost unchanged with the jet Reynolds number. These results also provide a measure of comparability of the jet character generated in the present experimental set-up. It may be noted that a virtual origin at zero is used to plot all the present data for this study.

**Table 1. Validation of decay constant ( $B$ ) and spreading rate ( $S$ ) for the turbulent jet with the earlier results.**

Parameters	Present experiment [ADV]	PANCHAPAKESAN and LUMLEY [23] [FHWA]	HUSSEIN <i>et al.</i> [3] [SHWA]
$Re_j$	22000	11000	95500
$x_0/d$	0	0	
$B$	5.90	6.06	5.90
$S$	0.101	0.096	0.102

Figure 4 represents the axial mean velocity profiles as a function of vertical distance ( $z/h$ ) at different downstream positions for jet Reynolds numbers  $Re_j = 8000, 15000$  and  $22000$  for the jet surface interaction case.  $z/h$  is the normalized vertical distance where  $z$  signifies the vertical distances of the measurement locations and  $h$  is the total water depth. BALL *et al.* [2] reported that the flow field of a free turbulent round jet is categorized into three distinct regions: core region, shear layer region and an outer region (shown in Fig. 5). Different axial zones of a free jet are also defined as the near field (usually within  $0 \leq x/d \leq 10$ ), the intermediate field ( $10 \leq x/d \leq 25$ ), and the far field ( $25 \leq x/d \leq$  breakdown location) [2]. In this present experiment, the flow field of a free turbulent jet also showed three distinct regions (not shown here). Whereas for the jet surface interaction cases the outer region of the lower part of the jet vanishes due to the rigid surface interaction. The shear layer region of the lower part also is observed to shrink due to the surface interaction (Fig. 5). It is pertinent that the upper portion of the jet is unaffected, while the centerline velocity is affected though faintly due to the influence of the rigid surface interaction (please see Fig. 4). Thus, it is clear that the influence of the rigid surface interaction is not efficient in penetrating through the core region of the jet.

It is evident from Fig. 5a that the mean axial velocity follows the Gaussian distribution at the near field ( $x/d = 5$ ) of the jet. Whereas it shifts from the Gaussian distribution for further downstream locations (Figs. 5b–f,  $x/d = 10$ –50). It may be noted that the flow at the near field of the jet is not interacting with the flat rigid bed, while from  $x/d = 10$  to 50 the rigid surface affects the jet structure. BALL *et al.* [2] stated that the capability to manage

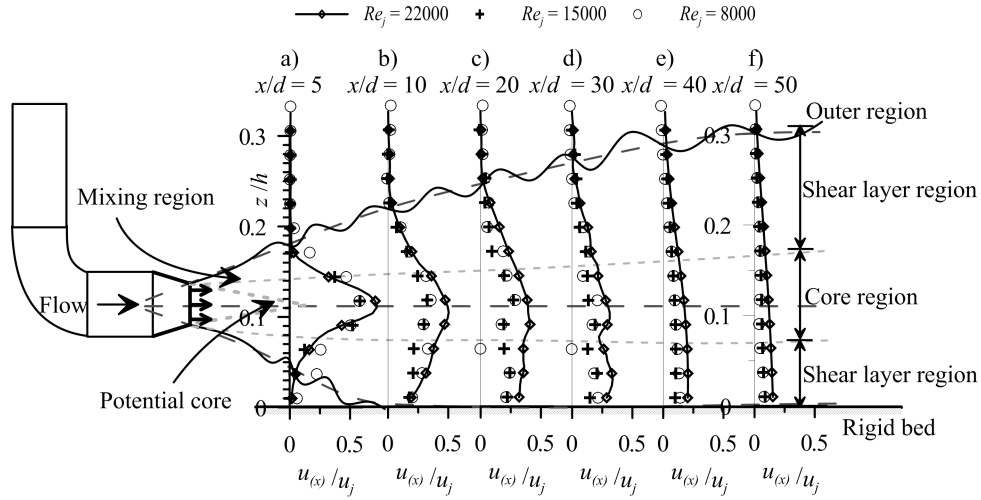


FIG. 5. The axial mean velocity profiles ( $u(x)/u_j$ ) as a function of vertical distance ( $z/h$ ) at different axial downstream locations for jet Reynolds numbers  $Re_j = 8000, 15000, 22000$ .

the flow development in the near to intermediate field of the jet have a very important relevance to many engineering purposes such as jet noise and mixing. In the present experiment, we have generated a scenario where the turbulent jet flow is being modulated by the rigid surface interaction development in the near to intermediate field of the jet at the lower portion of the jet shear layer.

## 6.2. Streamwise rms velocity distribution

Figures 6a–f show the vertical profiles of the streamwise rms velocity ( $u_{rms}$ ) for jet Reynolds numbers  $Re_j = 8000, 15000, 22000$  at different axial distances  $x/d = 5, 10, 20, 30, 40$  and  $50$ . The maximum value of  $u_{rms}$  is noticed at the shear layer regions near the orifice exit for free jets issuing in the quiescent background and it decreases with increasing axial distances [24]. Note that the  $u_{rms}$  profiles for different jet Reynolds numbers show a similar trend since the profiles are normalized by the corresponding jet discharge velocity. In Fig. 6 it is observed that the  $u_{rms}$  increases due to rigid surface interaction within the intermediate region near the rigid surface  $x/d = 10$  to  $30$  for all the three jets. It is clear that the  $u_{rms}$  is maximum for  $Re_j = 8000$  and decreases with increasing jet Reynolds numbers (i.e.,  $Re_j = 15000$  and  $22000$ ) at the near surface region ( $z/h \approx 0.08$ , Figs. 6c and d). Thus, it can be stated that the jet and rigid surface interaction modulate a wide range of axial velocity fluctuations within the intermediate region of the jet.

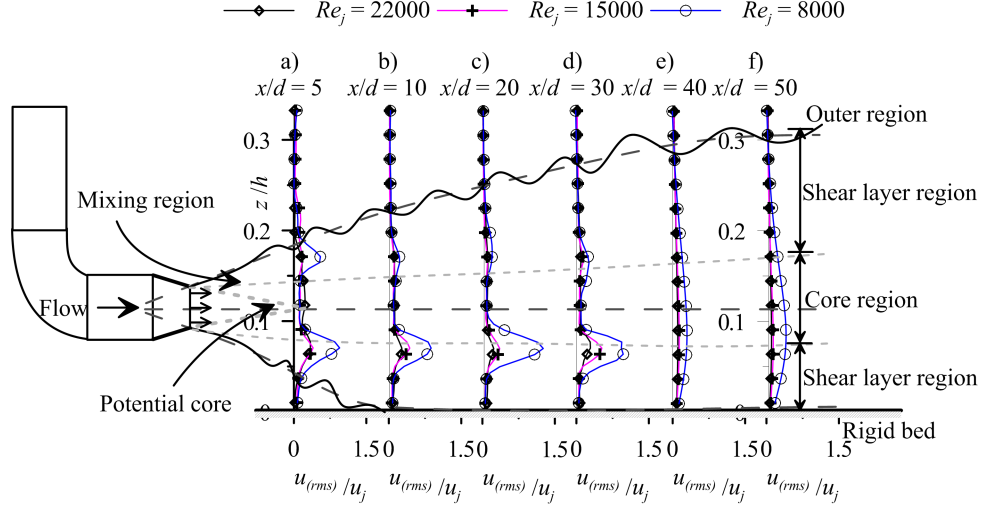


FIG. 6. The streamwise rms velocity profiles ( $u_{(rms)}/u_j$ ) as a function of vertical distance ( $z/h$ ) at different axial downstream locations for jet Reynolds numbers  $Re_j = 8000, 15000, 22000$ .

### 6.3. Reynolds shear stress distribution

Figure 7 represents the vertical profiles of Reynolds shear stress ( $\tau_{(uw)}/u_j^2$ ) at different  $x/d$  for the surface interacting jet Reynolds numbers  $Re_j = 8000, 15000, 22000$ . It is clear from Figs. 7a–f that, near the orifice, the  $\tau_{(uw)}/u_j^2$  shows the maximum value at the interfacial region of the core and shear layer region and the minimum value is observed at the centerline of the jet flow. It is observed that the highest value of shear stress appears at  $x/d = 30$  for the jet  $Re_j = 8000$  (Fig. 7d). The positive values of shear stress indicate the downward momentum flux in the negative  $z$  direction and the negative values of shear stress indicate the upward momentum flux in the positive  $z$  direction.

It is noted that the jet of  $Re_j = 8000$  shows the higher value of  $\tau_{(uw)}/u_j^2$  compared to  $Re_j = 15000$  and  $22000$  at all the axial locations. Shear stress arises when there is a mean velocity gradient in the direction transverse or normal to the flow [25]. It is evident from Fig. 4d that the velocity gradient for  $Re_j = 8000$  at  $x/d = 30, z/h = 0.06$  to  $0.1$  is greater than that of  $Re_j = 15000$  and  $22000$ . It is obvious that the higher velocity gradient can enhance the turbulence levels, which may amplify the shear stress at that particular region. It may be noted that a rigid surface restricts the flow velocity at the near surface region, resulting in an increase of the mean velocity gradient between the lower part of the jet shear layer and the core region of the jet. Possibly the lower Reynolds number flow is offered maximum surface restriction resulting in a steeper velocity gradient and

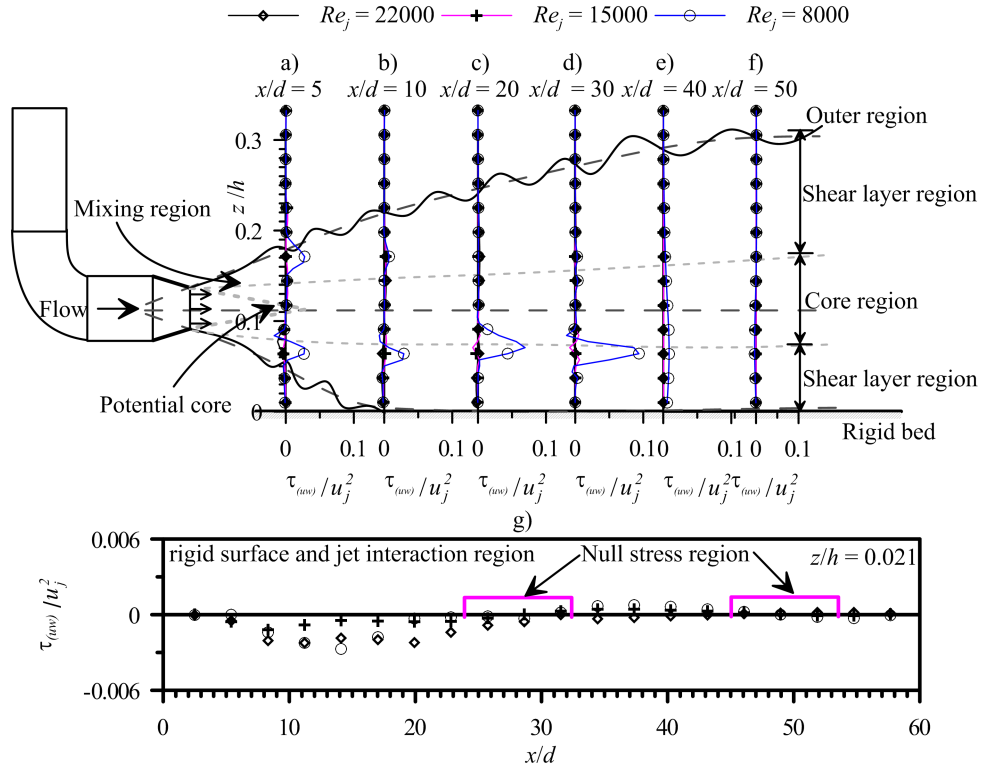


FIG. 7. a)–f) the profiles of  $(\tau_{(uw)}/u_j^2)$  as a function of vertical distance ( $z/h$ ) at different downstream locations; g) axial profiles of  $\tau_{(uw)}/u_j^2$  at the rigid surface and jet interaction region ( $z/h = 0.021$ ) for jet Reynolds numbers  $Re_j = 8000, 15000, 22000$ .

hence greater turbulence production and is manifested by the flow as the greater turbulent fluctuation variance.

Figure 7g represents the axial profiles of  $\tau_{(uw)}/u_j^2$  at  $z/h = 0.021$  (a closest measurable point near the rigid surface) for jet Reynolds numbers  $Re_j = 8000, 15000, 22000$ . It is noted that the upward momentum fluxes towards the positive  $z$  direction appear within the intermediate region of the jet for all the three jet Reynolds numbers ( $x/d = 10$  to  $25$ , Fig. 7g). Zero value of shear stress depicts the null stress zone within  $x/d = 25$  to  $35$ . Further, the downward momentum fluxes towards the negative  $z$  direction appear within  $x/d = 35$  to  $45$ . Another null stress zone is also pertinent for  $x/d = 45$  to  $55$ . It may be stated that first of all when the lower portion of the jet touches the rigid surface, the flow gets restricted by the bottom rigid surface; hence the upward momentum flux towards the positive  $z$  direction occurs. While the momentum flux is not able to propagate through the core region of the jet being the high energy region, and

hence the momentum flux gets reflected back from the core region of the jet; therefore the downward momentum flux occurs in the far field. The null stress occurs at the transition region (from upward to downward) of the momentum flux.

#### 6.4. Mixing length distribution

The mixing length ( $\hat{L}_m$ ) is computed as POPE [20]

$$(6.2) \quad \hat{L}_m = (|\overline{u'(x)w'(z)}|)^{0.5} / |\partial u(x)/\partial z|.$$

Figures 8a–f show the profiles of ( $\hat{L}_m$ ) as a function of vertical distance ( $z/h$ ) at different downstream locations for jet Reynolds numbers  $Re_j = 8000, 15000, 22000$ . It is anticipated that the rigid surface interacting jet has complex coherent turbulent structures due to the existence of surface generated eddies and vortices and therefore the movement of the turbulent flow is governed by packets of the fluid molecules instead of the activities of individual molecules. In view of the rigid surface interacting jet flow near the rigid surface as shown in Fig. 8, the mixing length values are more at  $x/d = 40$  (Fig. 8e) than that in the other locations.

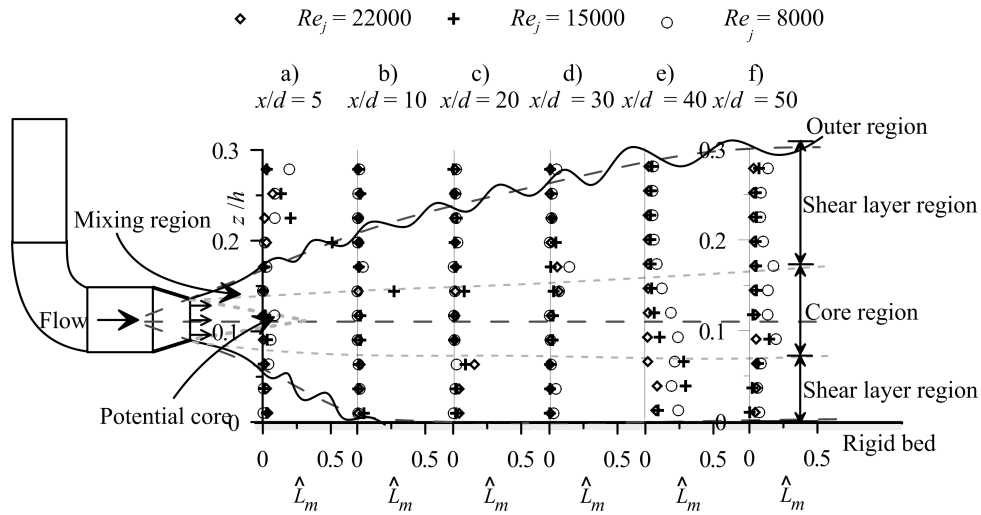


FIG. 8. a)–f) the profiles of ( $\hat{L}_m$ ) as a function of vertical distance ( $z/h$ ) at different downstream locations for jet Reynolds numbers  $Re_j = 8000, 15000, 22000$ .

It can be noted that the mixing length at  $x/d = 40$  (Fig. 7e) depicts the maximum length, a packet of fluid be capable of moving vertically; persevering its time-averaged velocity unaffected. It is evident from Fig. 6e and g that beyond  $x/d = 40$  the momentum flux changes direction from upward to downward

direction. The zone of the momentum flux direction change is characterized by increased dissipative scale eddies (eddy breakdown). This is also revealed from the velocity fluctuation variance plots (Figs. 6 and 7) in those locations resulting in unchanged streamwise mean velocity (also seen in Fig. 5). Thus the mixing length values are increased at that particular region signifying that fluid parcels have to travel larger vertical distance for gain or loss of momentum.

### 6.5. Distribution of TKE flux

The streamwise and vertical components of TKE flux are respectively defined as:

$$(6.3) \quad \begin{cases} f_{ku} = \frac{(\overline{u'(x)u'(x)u'(x)} + \overline{u'(x)v'(y)v'(y)} + \overline{u'(x)w'(z)w'(z)})/2}{u_j^3}, \\ f_{kw} = \frac{(\overline{w'(z)w'(z)w'(z)} + \overline{w'(z)u'(x)u'(x)} + \overline{w'(z)v'(y)v'(y)})/2}{u_j^3}. \end{cases}$$

The profiles of  $f_{ku}$  and  $f_{kw}$  are plotted against the normalized vertical distance  $z/h$  in Fig. 9 at a constant axial distance  $x/d = 30$  for the surface interacting jet of  $Re_j = 8000$ , 15000 and 22000. Particular  $x/d = 30$  is selected because the null stress occurs at that particular location (Fig. 7g), the flow structure and the distribution of kinetic energy flux may have some significant information at that location. The negative value of  $f_{ku}$  indicates that the energy is transported towards the downstream. Whereas the positive value of  $f_{kw}$  indicates the energy transported towards the upper surface.

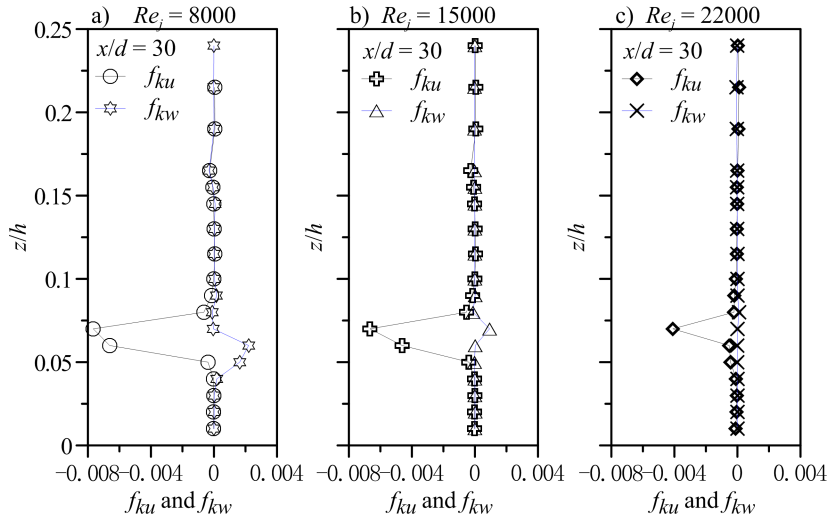


FIG. 9. The distributions of the TKE fluxes of  $f_{ku}$  and  $f_{kw}$  against  $z/h$  at the location  $x/d = 30$ ; a) for the surface interacting jet of  $Re_j = 8000$ ; b)  $Re_j = 15000$ ; c)  $Re_j = 22000$ .

It is clear from Figs. 9a–c that  $f_{ku}$  shows a negative value between the jet core region and shear layer region for  $z/h \approx 0.06$  to  $0.07$  and that is almost zero for other regions within the jet for all the three jet Reynolds numbers ( $Re_j = 8000, 15000$  and  $22000$ ). However, the distribution of  $f_{kw}$  shows positive values at the same location  $z/h \approx 0.06$  to  $0.07$  where  $f_{ku}$  shows a negative value. The negative  $f_{ku}$  and positive  $f_{kw}$  jointly generate a dawdling process. The propagation of stream-wise TKE flux opposite to the flow direction signifies that the inertia of the flowing fluid layer actuates a backoff effect wherein, a slowly moving fluid parcel appears in that particular region.

### 6.6. Near surface statistics

It is clear from the above discussion that, the interaction between the rigid surface generated eddies and diffused jet eddies within the lower portion of the jet shear layer modulates the flow and turbulence field, and the turbulence statistics of the interaction field is largely unknown. In this section we attempt to characterize the lower interaction zone of the jet based on the turbulence parameters such as the normalized turbulent kinetic energy, turbulent dissipation, velocity-derivative skewness and the enstrophy production using the expressions as detailed below:

Turbulent kinetic energy is calculated as:

$$(6.4) \quad k = 0.5(\overline{u'_{(x)}u'_{(x)}} + \overline{v'_{(y)}v'_{(y)}} + \overline{w'_{(z)}w'_{(z)}})/u_j^2.$$

The turbulent dissipation ( $\varepsilon$ ) is estimated as [3]:

$$(6.5) \quad \varepsilon = 15\nu\overline{(\partial u'_{(x)}/\partial x)^2}.$$

The production of turbulent kinetic energy ( $t_p$ ) is computed similar to MONIN and YAGLOM [26] as:

$$(6.6) \quad t_p = -\overline{u'_{(x)}w'_{(z)}}(\partial u_{(x)}/\partial z).$$

Integral scales ( $l_s$ ) are evaluated as:

$$(6.7) \quad l_s = \varepsilon^{3/2}/k.$$

The enstrophy production ( $E_n$ ) is estimated herein similar to PARK and CHUNG [27] and is given by:

$$(6.8) \quad E_n = -35\nu D \quad \text{where } D = \overline{(\nabla u_{(x)})^3}.$$

The velocity-derivative skewness ( $S_d$ ) is defined as [27]:

$$(6.9) \quad S_d = -\left(E_n \frac{3\sqrt{15}}{7} \frac{k}{\varepsilon^2}\right)/R_t^{0.5}.$$

Here  $R_t (\equiv k^2/\nu\varepsilon)$  is the turbulent Reynolds number.

Figures 10a, b and c show the contour plots of the normalized turbulent kinetic energy ( $k/u_j^2$ ); Figs. 10d, e, and f represent the contour plots of turbulent dissipation ( $\varepsilon(x - x_0)/u_j^3$ ). Moreover, Figs. 10g, h, and i show how the velocity-derivative skewness ( $S_d$ ) contours and finally, Figs. 10j, k, and l represent the enstrophy production ( $E_n(x - x_0)^2/u_j^4$ ) for jet Reynolds numbers  $Re_j = 8000, 15000, 22000$ .

The contours have been shown in the region close to the rigid surface for  $z/h = 0.01$  to  $0.06$ , to emphasize on the interaction zone extending  $x/d = 5$  to  $60$  in the longitudinal direction. These contour plots as shown in Fig. 10 displays the turbulence characteristics in the zone of interaction of the jet with the rigid surface primarily for broad qualitative behavior. In Fig. 11 the comparison of the above turbulence parameters have been made between jets with  $Re_j = 8000, 15000$  and  $22000$  and their rigid bed interaction at a longitudinal distance  $x/d = 30$  for quantitative assessment. It may be noted here that at  $x/d = 30$  is characterized by null stress (Fig. 7g).

TORDELLA *et al.* [28] stated that the turbulence spreading occurs due to the fluctuating pressure and velocity fields. The gradient of turbulent kinetic energy and integral scale usually depicts the inhomogeneity in the turbulence field. Figures 11a, b and c shows that the region  $z/h = 0.045$  to  $0.06$  is characterized as the high kinetic energy ( $k_h$ ) region, while the region below, i.e.,  $z/h = 0.045$  to  $0.01$  is characterized as the low kinetic energy ( $k_l$ ) region (also shown in Fig. 11a). TORDELLA *et al.* [28] reported that mixing layer is generated in the transition region between the high energy and low energy regions. Thus, it may be noted that a thin mixing layer is generated within  $z/h \approx 0.04$  to  $0.045$ ; due to the jet and rigid surface interaction. Careful examination of Fig. 10a reveals that a sharp change in the gradient of  $k/u_j^2$  occurs in this region which probably explains this artifact. Examination of Figs. 10d, e and f and Fig. 11b reveals that the zone of high turbulent kinetic energy is also a zone of high dissipation rate. It may be pointed out here that the mixing layer acts like a shield which restrains the penetration of the dissipative scale eddies.

Figure 11c displays the vertical profiles of the integral scales ( $l_s$ ) at constant  $x/d = 30$ . TORDELLA and IOVIENO [29] reported that, when the kinetic energy  $k_h/k_l$  ratio and the integral scale  $l_{sh}/l_{sl}$  ratio is consistent, the intermittency level and the depth of penetration by the eddies from the high-energy region increase; otherwise they decrease. The energy and length scale gradients were estimated for this study and it was observed that the calculated values are not concordant. Hence, it is anticipated that the depth of penetration of the eddies from the high-energy region decreases significantly at the mixing layer region.

From Figs. 7e, g it is clear that null stress region is developed at  $x/d = 30$ ,  $z/h = 0.045$ . GILBERT [30] stated that the production of turbulent kinetic energy

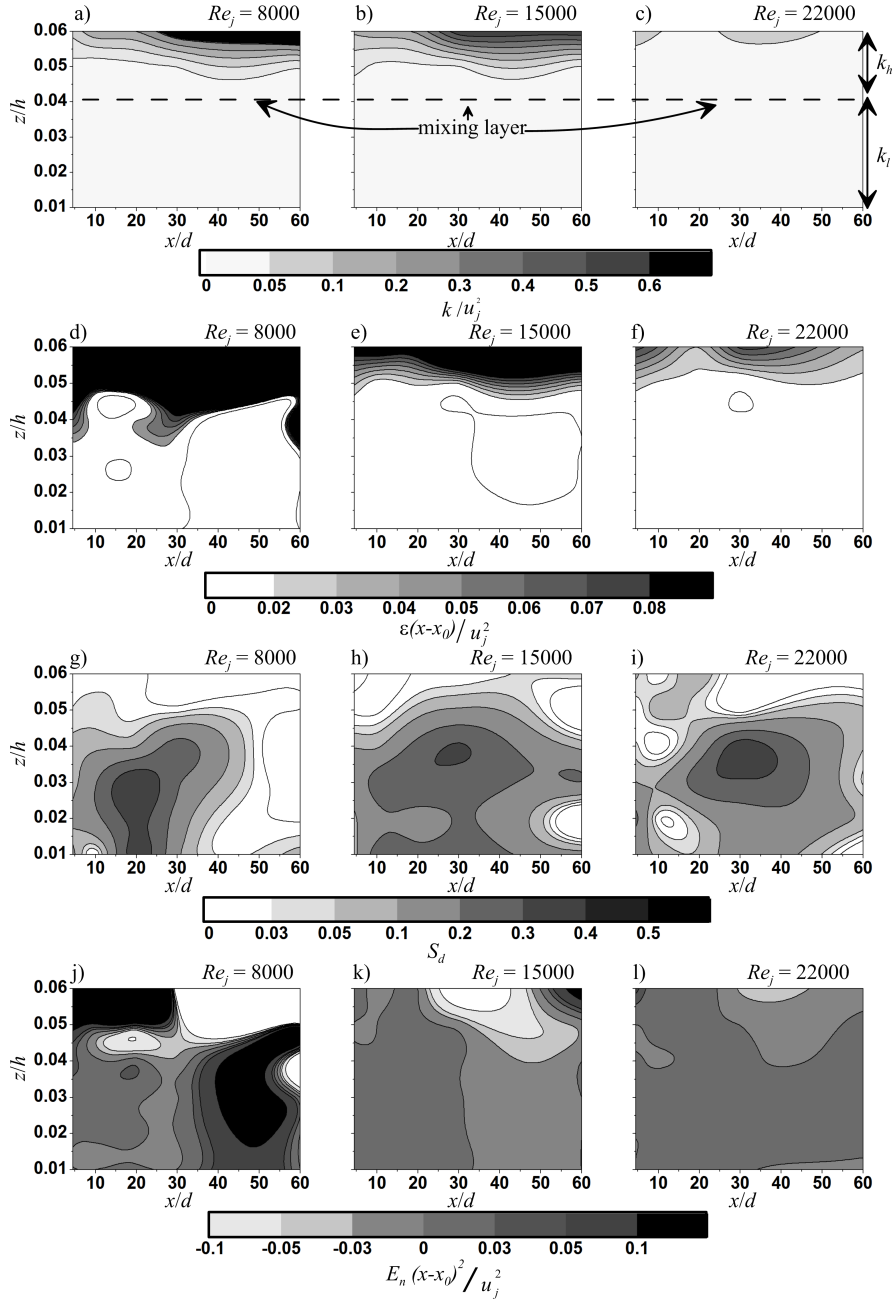


FIG. 10. (a, b and c) display the contour plots of the normalized turbulent kinetic energy ( $k/u_j^2$ ); (d, e and f) show the turbulent dissipation ( $\varepsilon(x-x_0)/u_j^3$ ); (g, h, and i) represent the velocity-derivative skewness ( $S_d$ ) contours; (j, k and l) the enstrophy production ( $E_n(x-x_0)^2/u_j^4$ ) at  $z/h = 0.01$  to  $0.06$ ,  $x/d = 5$  to  $60$  for the surface interacting jet of  $Re_j = 8000, 15000, 22000$ .

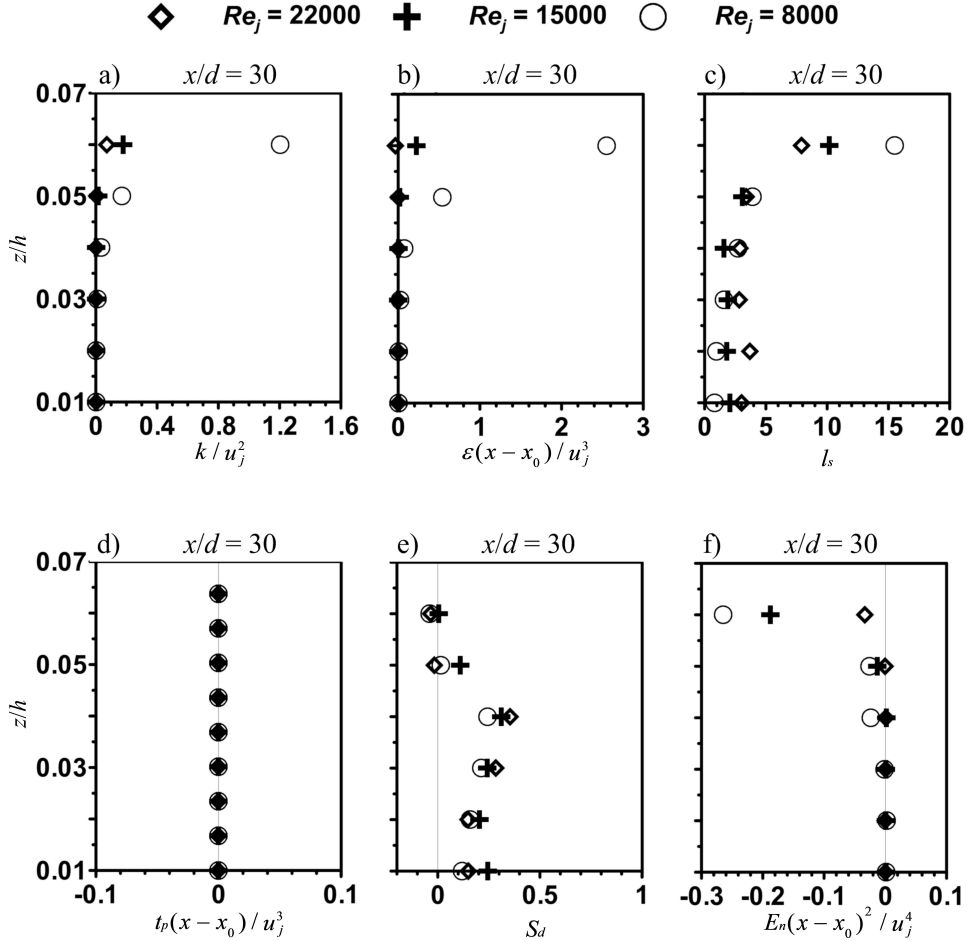


FIG. 11. The distributions of: a) the normalized turbulent kinetic energy ( $k/u_j^2$ ); b) turbulent dissipation ( $\varepsilon(x-x_0)/u_j^3$ ); c) integral scales ( $l_s$ ); d) the production of turbulent kinetic energy ( $t_p$ ); e) the velocity-derivative skewness ( $S_d$ ); f) the enstrophy production ( $E_n$ ) against  $z/h$  at the location  $x/d = 30$  for the surface interacting jet of  $Re_j = 8000, 15000, 22000$ .

and mean convective transport is absent in the shear less mixing region. Thus, it may be conceived that the mixing at this region is characterized as shear less mixing. Figure 11d presents the vertical distributions of normalized kinetic energy production ( $t_p(x-x_0)/u_j^3$ ) at  $x/d = 30$ . It is clear from Fig. 11 d that the kinetic energy production is almost zero within  $z/h = 0.01$  to  $0.06$  for all three jet Reynolds numbers. Thus for the present study, the region below the mixing layer can be treated as the shear less mixing region.

Figures 10g, h, and i and Fig. 11e represents the distributions of velocity-derivative skewness ( $S_d$ ) as a function of  $z/h$  for three different jets Reynolds

numbers. Generally, the velocity-derivative skewness ( $S_d$ ) signifies the rate of production of vorticity through vortex stretching [31]. It is evident from the contour plots that  $x/d = 30$  is characterized by the largest  $S_d$  and that vorticity also is being produced from the bottom. Careful observation of Fig. 11 shows that the rate of production of vorticity is enhanced due to vortex stretching and is caused by the nonlinear interactions between the jet bottom shear layer and the rigid surface. Moreover, the  $S_d$  starts to increase from  $z/h = 0.01$  and reaches a maximum value at  $z/h = 0.04$ , then it begins to decrease and shows zero value in the mixing layer. This result is in conformity to the previous results.

Figures 10j, k and l represent the enstrophy production ( $E_n(x - x_0)^2/u_j^4$ ) for surface interacting jets of  $Re_j = 8000, 15000$  and  $22000$ . For  $E_n > 0$ , the mean enstrophy production (vortex stretching) dominates over enstrophy destruction (vortex compression) [31]. Drawing an analogy from the above it is observed from Fig. 11f that the mean enstrophy production is favored over enstrophy destruction starting from  $z/h = 0.01$  up to the mixing layer ( $z/h \approx 0.045$ ). Further, it is observed that  $E_n < 0$  starting from the mixing layer region up to  $z/h = 0.06$ . Thus, it may state that the enstrophy destruction is favored over enstrophy production at the upper portion of the mixing layer. Though the contour plots (Figs. 10j, k, and l) show complex distribution but qualitatively the above artifact is more prominently justified in the plots.

### 6.7. Distribution of turbulent eddies

It is gestated from the above results and discussions that the rigid surface considerably modulates the eddy structure inside the jet flow field, more specifically in the lower portion of the jet shear layer. In order to highlight the distinctiveness of eddy scale distributions based on the velocity fluctuations, the wavelet analysis is presented herein. WANG *et al.* [13] stated that the wavelet analysis of random signals is capable of giving information on the eddy scale and their associated occurrence frequency. Further, for large Reynolds number flows the length scale of eddies illustrate a broad range of the spectral band [19]. The current experiments were carried out with large jet Reynolds numbers ( $Re_j = 8000, 15000, 22000$ ). The wavelet analysis shows the velocity signal in the wavelet scale or pseudo-frequency ( $f$ ) which is extracted by disintegrating the signal into the flexibly-sized time casement. In wavelet analysis, the scale to frequency is associated to determine the central frequency of the wavelet,  $f_{ct}$ , based on the following relationship:  $f = f_{ct}/d \cdot \Delta$  where,  $d$  is a scale;  $\Delta$  is the sampling period;  $f_{ct}$  is the center frequency of a wavelet in Hz;  $f$  is the pseudo-frequency corresponding to the scale  $d$ , in Hz. The concept is to relate a purely periodic signal of frequency  $f_{ct}$  with a given wavelet. The time information can be acquired by the short-time Fourier transform but the range of the time window is constant

for this purpose. Continuous wavelet transforms (CWT) of a signal  $s(t_i)$  may be characterized by a family of wavelet functions [19], that can be written as:

$$(6.10) \quad \varpi(l, d) = \frac{1}{\sqrt{d}} \int_{-\infty}^{\infty} s(t_i) \psi^* \left( \frac{t-r}{d} \right) dt,$$

where  $\varpi$  is the wavelet coefficient;  $l$  is the position (time or space);  $d$  is the wavelet scale; the  $*$  symbol represents the conjugated value;  $\psi$  is the mother wavelet function [13]. The wavelet function is capable of expanding and changing the scale  $d$  and hence investigates the location  $t$ , that corresponds to a particular scale of  $d$ . The Fast Fourier Transform (FFT) of a convolution in the time domain equals the point-wise multiplication in the frequency domain [13]. Hence, the wavelet coefficient  $\varpi$  physically suggests the degree of correspondence between signal  $s(t_i)$  and the wavelet function. It is the simplest tool to study the whole signal at different scales and positions in time or space domain by altering the parameters  $d$  and  $l$ . An eddy can be explained as a function of time and scale (frequency) through the wavelet coefficient [19, 32]. Further, the location of the highest valued wavelet coefficient depicts the large-scale eddy. The Morlet wavelet is applied herein to distinguish the eddy scales based on the magnitudes of the wavelet coefficients (similar to ROY *et al.* [19]).

FARGE *et al.* [40] noted that Local Intermittency Measure (LIM) is capable of locating discrete events within a given time series; particularly those events producing intermittency. The LIM is defined as follows:

$$(6.11) \quad LIM_{l,d} \equiv \frac{|\varpi(l, d)|^2}{\langle |\varpi(l, d)|^2 \rangle_l},$$

where  $|\varpi(l, d)|^2$  is the local energy density at the scale  $d$  and  $\langle |\varpi(l, d)|^2 \rangle_l$  is the average value of the energy density at the same scale  $d$ . It may be noted that the  $LIM_{l,d}$  represents the local activity of the signal  $s(t_i)$  at each scale  $d$ . In an alternative way,  $LIM_{l,d}$  is equivalent to the Fourier spectrum. The condition  $LIM_{l,d} = 1$  represents that within the signal  $s(t_i)$ , each segment of it has the same energy spectrum that corresponds to the Fourier spectrum, that does not show intermittency. Conversely,  $LIM_{l,d} > 1$  locate those segments of the signal  $s(t_i)$ , that have more power than they should have in case they were normally distributed. Consequently, the condition  $LIM_{l,d} > 1$  allows us to locate intermittent events in time and eddy scale ( $d$ ). These events can be extracted from the original time series. CONSOLINI and MICHELIS [48] used this method to track the global high-latitude geomagnetic activity.

Figures 12b and f display the snapshot of the distribution of eddies for a constant time window ( $t = 35000$  milliseconds) based on the distribution of wavelet

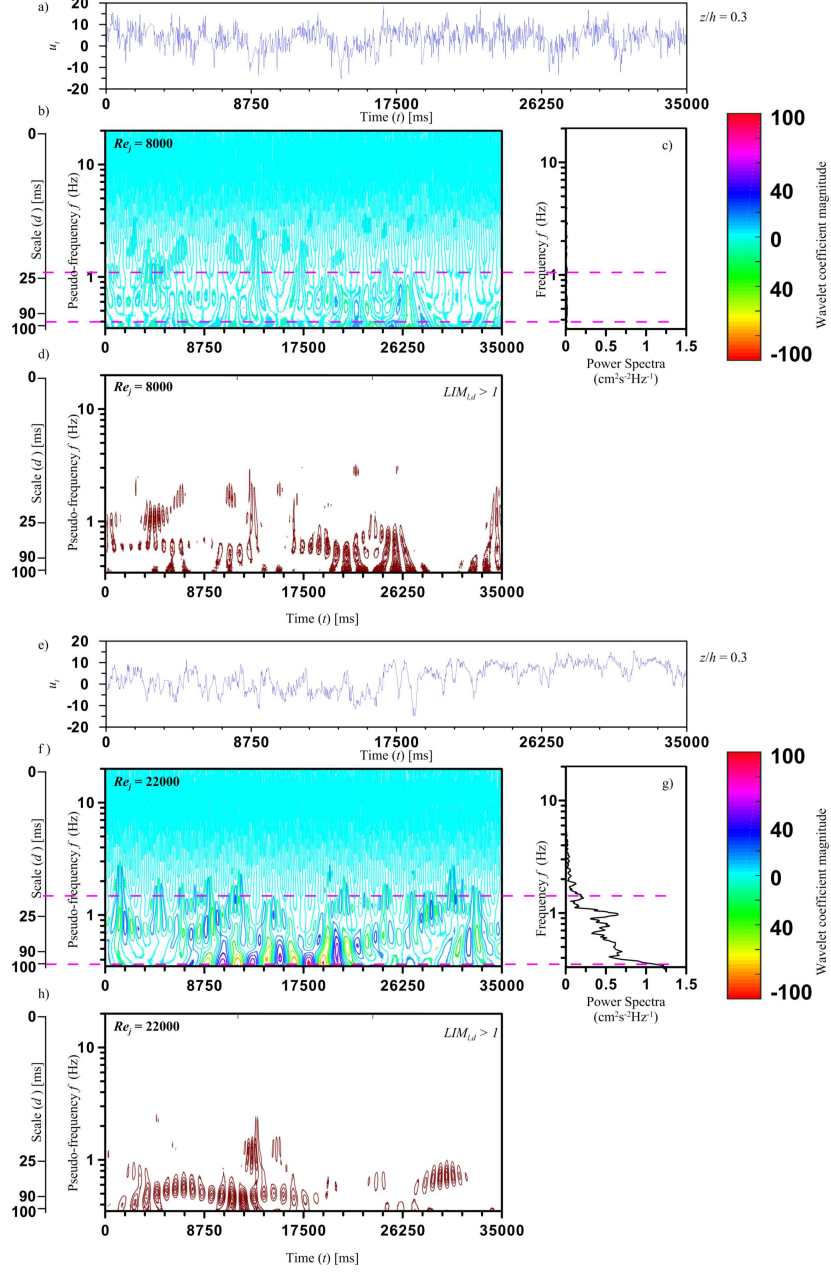


FIG. 12. (a and e) display the instantaneous velocity plots as a function of time ( $t$ ); (b and f) wavelet coefficient contours in pseudo frequency and time plane; (c and g) FFT output; (d and h) Local Intermittency Measure for condition  $LIM_{l,d} > 1$ ; at levels ( $z/h = 0.3$ ) and a fixed  $x/d = 30$  for the surface interacting jet of  $Re_j = 8000$  and  $22000$ .

coefficients for the surface interacting jet of  $Re_j = 8000$  and  $22000$  at  $x/d = 30$ ,  $z/h = 0.3$  (the interfacial region between outer layer and upper shear layer). Figures 12a and e represent the raw velocity signal and Figs. 12c and g represent the FFT of the raw signal based on which the wavelet coefficients in Figs. 12b and f were computed [19, 32]. It is evident that at any particular time in the time window large scale and small scale eddies coexist and are randomly distributed within the time domain (Figs. 12b and f). The FFT output of those time segments (shown at the right of respective wavelet coefficient contours) shows large peaks at the frequencies where most of the large eddies exist. Figures 12d and h represent the Local Intermittency Measure (LIM) plots to locate discrete events within the time series measured at  $x/d = 30$ ,  $z/h = 0.3$ . Please note that the condition  $LIM_{l,d} > 1$  signifies those events which may produce intermittency (in the time domain) within the local flow field.

It may be noted here that the pseudo frequency ( $f$ ) axis of the wavelet coefficient contour and the FFT output frequency axis are plotted to identical scale parallel for direct assessment. It is revealed that the largest wavelet coefficient corresponds to a peak in frequency (or pseudo frequency). Here the wavelet coefficients are highly random; the large scale eddy regions are demarcated and bounded by two pink dashed lines. It is interesting to observe that small amount of large scale eddies are present at  $f = 0.4$  to  $1$  Hz (energy containing region of power spectral density, please see *Pope* [20] in the interfacial region between the jet outer layer and ambient fluid (Figs. 12b and f,  $z/h = 0.3$ ,  $x/d = 30$ ). It may be noted here that the rigid surface interaction is incapable of modulating the eddies at the upper interfacial region of the jet of  $Re_j = 8000$  and  $22000$  (discussed earlier). Thus, it may be stated that the characteristics of these eddies are quite similar to that for the free jet case at that particular region ( $z/h = 0.3$ ,  $x/d = 30$ ). Comparison between Figs. 12b and f reveal that larger Reynolds number produces larger eddies.

Figures 13b and f show the distribution of eddies for a constant time window ( $t = 35000$  milliseconds) based on the distribution of wavelet coefficients for the surface interacting jet of  $Re_j = 8000$  and  $22000$  at  $x/d = 30$ ,  $z/h = 0.12$  (i.e., core region of the jet). Figures 13 d and h represent the Local Intermittency Measure (LIM) plots with condition  $LIM_{l,d} > 1$  to locate discrete events within the time series measured at  $x/d = 30$ ,  $z/h = 0.12$ . It is found that, within the jet core region (Fig. 13b,  $z/h = 0.12$ ,  $x/d = 30$ ) combination of large and moderate scale eddies co-exist for the pseudo frequency range  $f = 0.3$  to  $10$  Hz for  $Re_j = 8000$  while  $Re_j = 22000$  the amalgamation of large and moderate scales of eddies are observed the pseudo frequency range  $f \approx 0.3$  to  $2$  Hz within the jet core region (Fig. 13f,  $z/h = 0.12$ ,  $x/d = 30$ ). Thus the large and moderate scale eddies are distributed at the energy containing region, inertial subrange and dissipative range [20] of power spectral density for  $Re_j = 8000$ . Whereas large

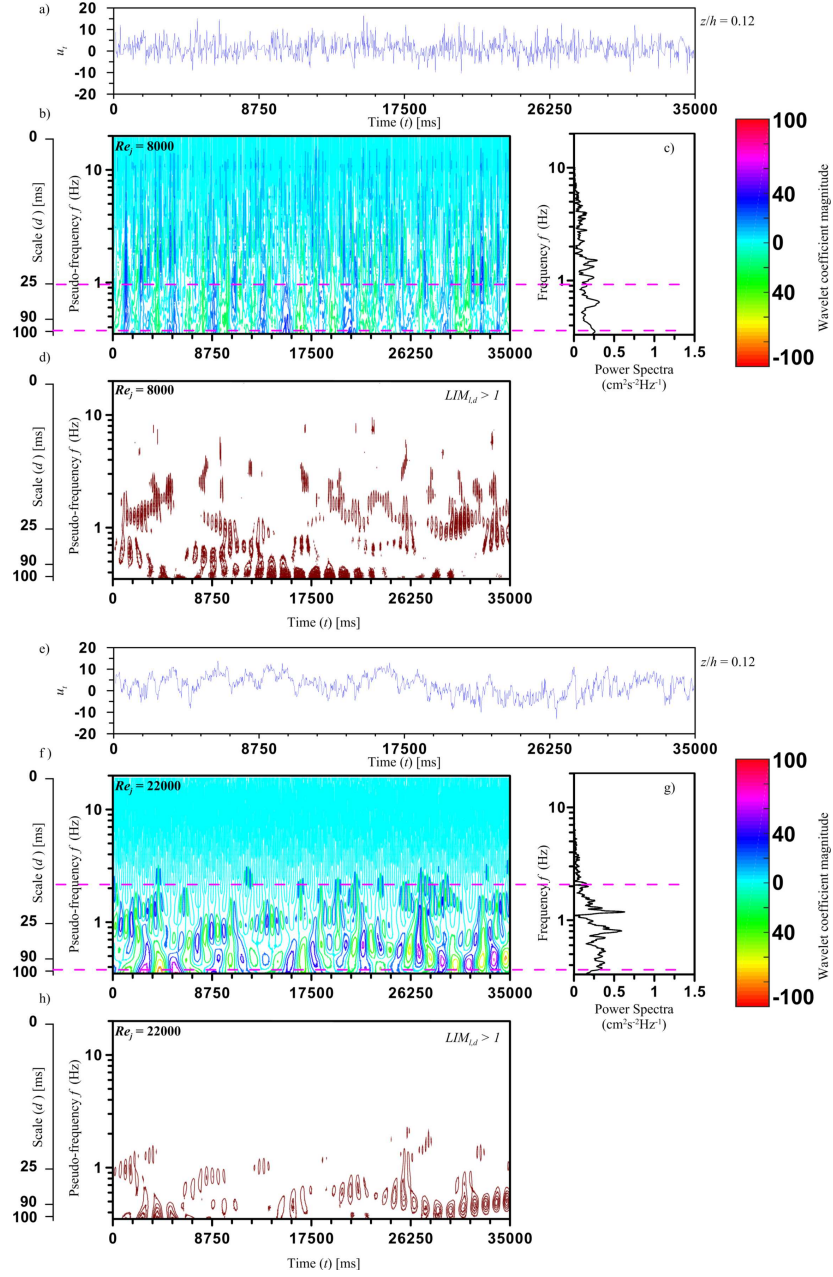


FIG. 13. (a and e) display the instantaneous velocity plots as a function of time ( $t$ ); (b and f) wavelet coefficient contours in pseudo frequency and time plane; (c and g) FFT output; (d and h) Local Intermittency Measure for condition  $LIM_{l,d} > 1$ ; at levels ( $z/h = 0.12$ ) and a fixed  $x/d = 30$  for the surface interacting jet of  $Re_j = 8000$  and  $22000$ .

and moderate scales of eddies are distributed at the energy containing region, inertial subrange of power spectral density for  $Re_j = 22000$ .

Figures 14b and f represent the distribution of eddies for a constant time window for the jet of  $Re_j = 8000$  and  $22000$  at  $x/d = 30$ ,  $z/h = 0.045$  (mixing layer region). Figures 14d and h display the condition  $LIM_{l,d} > 1$ , which may be used to locate the discrete events within the time series measured at  $x/d = 30$ ,  $z/h = 0.045$ . Interestingly, the maximum amount of large and moderate scale eddies are present at the pseudo frequency range  $f \approx 0.3$  to  $10$  Hz in the mixing layer region for the jet of  $Re_j = 8000$  (i.e. almost the whole spectral range). Careful scrutiny and comparison of Figs. 14b with 13b and 12b suggest that the size of the eddies have considerably increased in the mixing layer as compared to that of the core region and outer layer of the jet for  $Re_j = 8000$ . Similar observation is also revealed for  $Re_j = 22000$  (Figs. 14f with 13f and 12f). More specifically, the highest concentration of large scale and moderate eddies are distributed within the inertial subrange (Fig. 14b,  $f \approx 1$  to  $6$  Hz).

Figures 15b and f show the distribution of eddies for  $Re_j = 8000$  and  $22000$  at the null stress region, i.e.,  $x/d = 30$ ,  $z/h = 0.01$ . Figures 15d and h show  $LIM_{l,d} > 1$  in order to locate the discrete events within the time series measured at  $x/d = 30$ ,  $z/h = 0.01$ . It is found that, in the region close to the rigid surface, i.e., the direct interaction region of the jet and the rigid surface (Fig. 15b,  $z/h = 0.01$ ,  $x/d = 30$ ) high concentration of large-scale eddies exists at the pseudo frequency ranging from  $f = 0.3$  to  $0.7$  Hz for both jets with  $Re_j = 8000$  and  $22000$  (energy containing region of power spectral density as shown in [20]). Thus it is evident that the jet and the rigid surface interaction leads to the generation of some additional eddies at the near surface region of the jet. Comparison of Fig. 15b and 12b (for  $Re_j = 8000$ ); and Fig. 15f and 12f (for  $Re_j = 22000$ ) reveal that larger eddies are generated due to rigid surface interaction than at the jet outer layer.

The axial velocity distribution as a function of the vertical distances maintains the top-hat Gaussian distribution at the initial region of the jet (where the jet does not touch the rigid surface). Whereas the jet velocity structure departs from the top-hat Gaussian distribution at the intermediate and far field due to the rigid surface interaction (please see Fig. 5). Figure 16 displays the conceptual diagram of the axisymmetric turbulent jet interacting with a flat rigid surface (parallel to the jet axis) based on experimental data of the present study. It is observed that the mean velocity increases near the rigid surface (to maintain mass continuity), which may generate a strong velocity gradient between the core region and bottom shear layer. Due to this, different scales of eddies are formed and are distributed within the inertial subrange (in the frequency domain). As a result, the Reynolds shear stresses increase at this particular region. Moreover, the upper portion of this region is characterized as high TKE and the lower portion

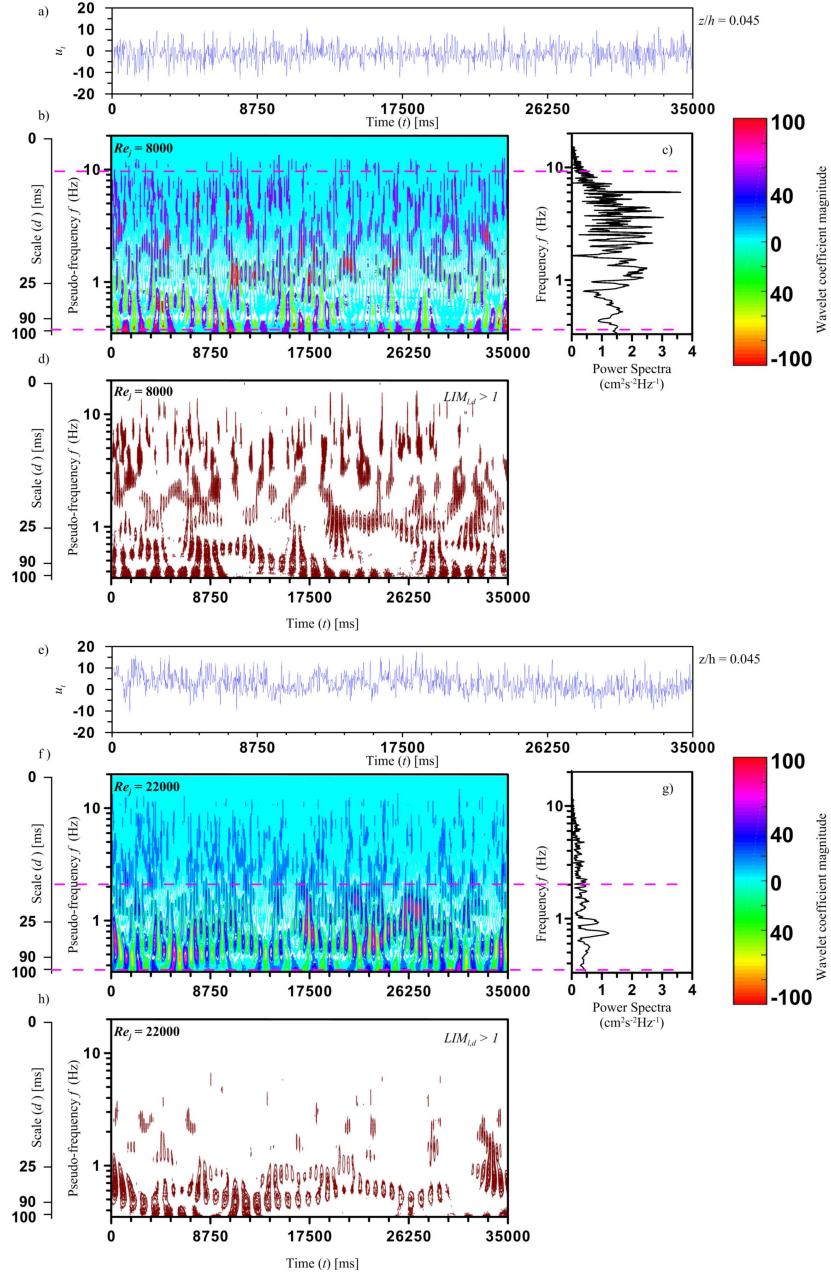


FIG. 14. (a and e) display the instantaneous velocity plots as a function of time ( $t$ ); (b and f) wavelet coefficient contours in pseudo frequency and time plane; (c and g) FFT output; (d and h) Local Intermittency Measure for condition  $LIM_{l,d} > 1$ ; at levels ( $z/h = 0.045$ ) and a fixed  $x/d = 30$  for the surface interacting jet of  $Re_j = 8000$  and  $22000$ .

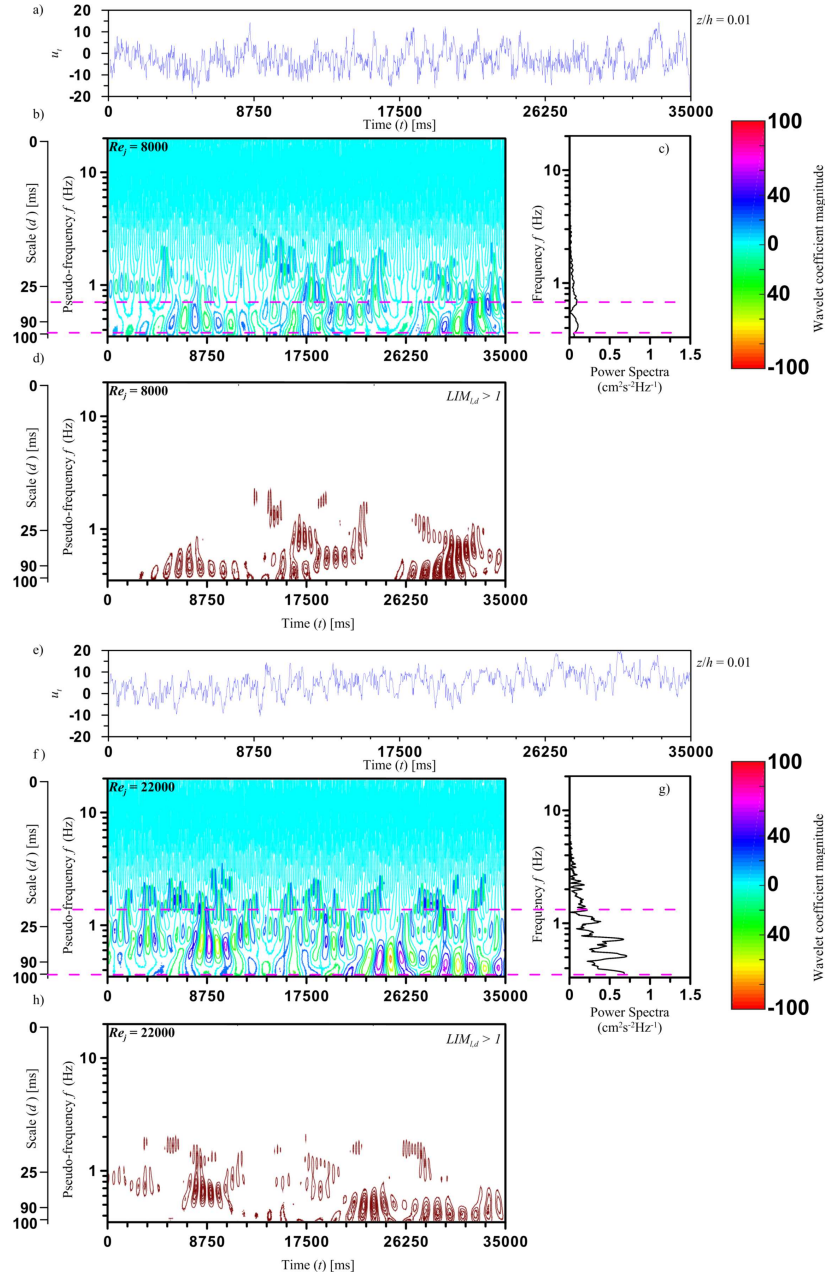


FIG. 15. (a and e) display the instantaneous velocity plots as a function of time ( $t$ ); (b and f) wavelet coefficient contours in pseudo frequency and time plane; (c and g) output; (d and h) Local Intermittency Measure for condition  $LIM_{l,d} > 1$ ; at levels ( $z/h = 0.01$ ) and a fixed  $x/d = 30$  for the surface interacting jet of  $Re_j = 8000$  and  $22000$ .

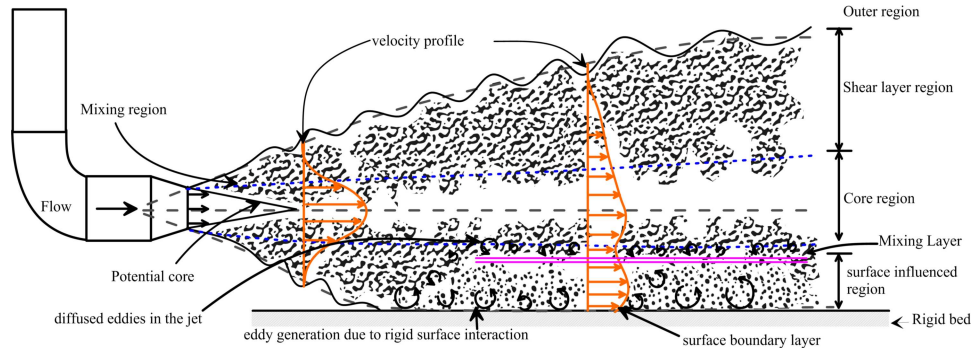


FIG. 16. The conceptual diagram of the turbulent jet interacting rigid surface.

is characterized as low TKE region (please see Figs. 10a–c, 11a). It is interesting to note that an additional mixing layer is formed at the interfacial region of high and low TKE regions, demarcated by the pink line in Fig. 16. It can be stated that the size of the eddies has considerably increased in the mixing layer as compared to that of in another region. The concentration of large-scale eddies in the mixing layer acts like a shield between the lower and the upper regions. Due to this, rigid surface generated eddies are incapable of penetration through the mixing layer and thus the upper portion of the turbulent jet remains unaffected.

## 7. Conclusions

The turbulent jet-surface interaction flows have been studied previously by many researchers, but no attempt has been made to investigate the turbulence statistics and the behavior of eddy structures in and around the turbulent jet impinging on the quiescent background parallel to a flat rigid surface.

The results of the present can be summarized as follows:

The turbulent structure of a jet flow is significantly modulated due to the rigid surface interaction; particularly within the lower portion of the jet shear layer.

The influence generated by the rigid surface interaction on the jet turbulence structure is not capable of propagating through the core region of the jet. Most importantly, the momentum flux generated from the rigid surface does not propagate through the core region of the jet. The jet and rigid surface interaction modulate a wide range of axial velocity fluctuations within the intermediate and far field of the jet in the longitudinal direction. LAUNDER and RODI [35] noted that for the turbulent wall jet (an orifice placed at the near most location on the wall), the values of lateral and bottom normal velocity gradients are small. The wall shear stress are capable of generating the streamwise vortices which

does not evolve towards the core region of the wall jet. Also, the peak velocity occurs further from the wall where the effective viscosity increases strongly with distance from the wall resulting in the vorticity-generation within the inner region. LAUNDER and RODI [35] stated that the shear stress does not vanish at the core region (maximum velocity region) but at the region closer to the wall (null stress region). This is yet another feature of a wall jet and this suggests that the magnitude of the vortices generated from the wall at the null stress region is smaller than the core region, and it has negligible effect on the flow structure at the core region. The results from the present study depicts similar phenomenon as stated by LAUNDER and RODI [35].

- The rigid surface interaction plays a significant role to alter the eddy structures through a dawdling process with the appearance of slowly moving fluid parcels in the lower inflection region (i.e., between the lower shear layer and core region) of the turbulent jet.
- The present study reveals that a new mixing layer is formed in the transition region between the high-energy region (i.e., within the jet core) and low energy region (i.e., within the lower portion of the jet shear layer).
- Results suggest that the region below the mixing layer can be treated as the shear less mixing region. The interesting consequence is that the rate of production of vorticity is maximum below the mixing layer. Also, the enstrophy destruction is favored over enstrophy production at the upper portion of the mixing layer, and this is opposite to that of the lower portion of the mixing layer. Finally, the jet and surface interaction produces the large-scale eddies near the rigid surface region which probably does not penetrate through the mixing layer.

## Acknowledgements

The author would like to acknowledge the Department of Science and Technology, Government of India for financial support for this research (File No. EMR/2015/MERC/000266.). The authors would also like to express their sincere gratitude to the anonymous reviewers for their comprehensive advise.

## References

1. J. MI, P. KALT, G.J. NATHAN, C.Y. WONG, *PIV measurements of a turbulent jet issuing from round sharp-edged plate*, Experiments in Fluids, **42**, 4, 625–637, 2007.
2. C.G. BALL, H. FELLOUAH, A. POLLARD, *The flow field in turbulent round free jets*, Progress in Aerospace Sciences, **50**, 1–26, 2012.
3. H.J. HUSSEIN, S.P. CAPP, W.K. GEORGE, *Velocity measurements in a high-Reynolds-number, momentum-conserving, axisymmetric, turbulent jet*, Journal of Fluid Mechanics, **258**, 31–75, 1994.

4. P.C. CHATWIN, C.M. ALLEN, *Mathematical models of dispersion in rivers and estuaries*, Annual Review of Fluid Mechanics, **17**, 1, 119–149, 1985.
5. A.J. BASU, R. NARASIMHA, *Direct numerical simulation of turbulent flows with cloud-like off-source heating*, Journal of Fluid Mechanics, **385**, 199–228, 1999.
6. A. AGRAWAL, B.J. BOERSMA, A.K. PRASAD, *Direct numerical simulation of a turbulent axisymmetric jet with buoyancy induced acceleration*, Flow Turbulence and Combustion, **73**, 3, 277–305, 2005.
7. I. WYGNANSKI, H. FIEDLER, *Some measurements in the self-preserving jet*, Journal of Fluid Mechanics, **38**, 3, 577–612, 1969.
8. D.M. CHASE, *Noise radiated from an edge in turbulent flow*, AIAA Journal, **13**, 8, 1041–1047, 1975.
9. R.W. HEAD, M.J. FISHER, *Jet/surface interaction noise-Analysis of farfield low frequency augmentations of jet noise due to the presence of a solid shield*, Third Aeroacoustics Conference, 1976.
10. J.L.T. LAWRENCE, M. AZARPEYVAND, R.H. SELF, *Interaction between a flat plate and a circular subsonic jet*, AIAA Journal, 2745, 2011.
11. C.A. BROWN, *Jet-surface interaction test: far-field noise results*, Journal of Engineering for Gas Turbines and Power, **135**, 7, 071201–071201, 2013.
12. K.B.M.Q. ZAMAN, C.A. BROWN, J.A. BRIDGES, *Interaction of a rectangular jet with a flat-plate placed parallel to the flow*, AIAA/CEAS Aeroacoustics Conference, **E-18684**, 2013–2184, 2013.
13. H. WANG, S. LEE, Y.A. HASSAN, A.E. RUGGLES, *Laser-Doppler measurements of the turbulent mixing of two rectangular water jets impinging on a stationary pool*, International Journal of Heat and Mass Transfer, **92**, 206–227, 2016.
14. J. MORLET, *Sampling theory and wave propagation*, Issues in Acoustic signal/Image Processing and Recognition, **1**, 233–261, 1983.
15. J. NIU, B. SIVAKUMAR, *Scale-dependent synthetic streamflow generation using a continuous wavelet transform*, Journal of Hydrology, **496**, 71–78, 2013.
16. V. SEHGAL, M.K. TIWARI, C. CHATTERJEE, *Effect of utilization of discrete wavelet components on flood forecasting performance of wavelet based ANFIS models*, Water Resources Management, **28**, 6, 1733–1749, 2014.
17. V. SEHGAL, M.K. TIWARI, C. CHATTERJEE, *Wavelet bootstrap multiple linear regression based hybrid modeling for daily river discharge forecasting*, Water Resources Management, **28**, 10, 2793–2811, 2014.
18. A. PANIZZO, G. BELLOTTI, P. DE GIROLAMO, *Application of wavelet transform analysis to landslide generated waves*, Coastal Engineering, **44**, 4, 321–338, 2002.
19. S. ROY, K. DEBNATH, B.S. MAZUMDER, *Distribution of eddy scales for wave current combined flow*, Applied Ocean Research, **63**, 170–183, 2017.
20. S.B. POPE, *Turbulent Flows*, Cambridge University Press, Cambridge, 2001.
21. N. RAJARATNAM, *Turbulent Jets*, Vol. 5, Elsevier, Amsterdam, 1976.
22. W.K. GEORGE, *The self-preservation of turbulent flows and its relation to initial conditions and coherent structures*, Advances in Turbulence, 3973, 1989.

23. N.R. PANCHAPAKESAN, J.L. LUMLEY, *Turbulence measurements in axisymmetric jets of air and helium, Part 1. Air jet*, Journal of Fluid Mechanics, **246**, 197–223, 1993.
24. S.J. KWON, I.W. SEO, *Reynolds number effects on the behavior of a non-buoyant round jet*, Experiments in Fluids, **38**, 6, 801–812, 2005.
25. A.A. SONIN, *Equation of Motion for Viscous Fluids*, Massachusetts Institute of Technology, Massachusetts, 2001.
26. A.S. MONIN, A.M. YAGLOM, *Statistical Fluid Mechanics, Vol. II: Mechanics of Turbulence*, Courier Corporation, Massachusetts, 2013.
27. J.Y. PARK, M.K. CHUNG, *An analytical model of velocity-derivative skewness of rotating homogeneous turbulence*, Fluid Dynamics Research, **26**, 5, 281–288, 2000.
28. D. TORDELLA, M. IOVIENO, P.R. BAILEY, *Sufficient condition for Gaussian departure in turbulence*, Physical Review E, **77**, 1, 016309–016309, 2008.
29. D. TORDELLA, M. IOVIENO, *Small-scale anisotropy in turbulent shearless mixing*, Physical Review Letters, **107**, 19, 194501–194501, 2011.
30. B. GILBERT, *Diffusion mixing in grid turbulence without mean shear*, Journal of Fluid Mechanics, **100**, 2, 349–365, 1980.
31. G.I. TAYLOR, *Production and dissipation of vorticity in a turbulent fluid*, Proceedings of the Royal Society of London Series A, Mathematical and Physical Sciences, 15–23, 1938.
32. H. LI, T. NOZAKI, *Wavelet analysis for the plane turbulent jet: analysis of large eddy structure*, JSME International Journal Series B, Fluids and Thermal Engineering, **38**, 4, 525–531, 1995.
33. C.D. WINANT, F.K. BROWAND, *Vortex pairing: the mechanism of turbulent mixing-layer growth at moderate Reynolds number*, Journal of Fluid Mechanics, **63**, 2, 237–255, 1974.
34. K.B. ZAMAN, A.K. HUSSAIN, *Vortex pairing in a circular jet under controlled excitation. Part 1. General jet response*, Journal of Fluid Mechanics, **101**, 3, 449–491, 1980.
35. B.E. LAUNDER, W. RODI, *The turbulent wall jet measurements and modeling*, Annual Review of Fluid Mechanics, **15**, 1, 429–459, 1983.
36. A. DI MARCO, M. MANCINELLI, R. CAMUSSI, *Pressure and velocity measurements of an incompressible moderate Reynolds number jet interacting with a tangential flat plate*, Journal of Fluid Mechanics, **770**, 247–272, 2015.
37. O. DE ALMEIDA, A.R. PROENÇA, R.H. SELF, *Experimental characterization of velocity and acoustic fields of single-stream subsonic jets*, Applied Acoustics, **127**, 194–206, 2017.
38. I. REBA, *Applications of the Coanda effect*, Scientific American, **214**, 6, 84–93, 1966.
39. M. FARGE, *Wavelet transforms and their applications to turbulence*, Annual Review of Fluid Mechanics, **24**, 395–457, 1992.
40. M. FARGE, *Wavelet analysis of coherent structures in two-dimensional turbulent flows*, Physics of Fluids A: Fluid Dynamics (1989–1993), **3**, 9, 2029, 1991
41. D. JR. PANDRES, *Derivation of admissibility conditions for wave functions from general quantum-mechanical principles*, Journal of Mathematical Physics, **3**, 305, 1962.
42. R. CAMUSSI, G. GUJ, *Orthonormal wavelet decomposition of turbulent flows: intermittency and coherent structures*, Journal of Fluid Mechanics, **348**, 177–199, 1997.

43. R. CAMUSSI, G. GUJ, *Experimental analysis of intermittent coherent structures in the near field of a high Re turbulent jet flow*, *Physics of Fluids*, **11**, 2, 423–431, 1999.
44. S. GRIZZI, R. CAMUSSI, *Wavelet analysis of near-field pressure fluctuations generated by a subsonic jet*, *Journal of Fluid Mechanics*, **698**, 93–124, 2012.
45. C.M. GARCÍA, M. CANTERO, Y. NIÑO, M.H. GARCÍA, *Turbulence measurements with acoustic Doppler velocimeters*, *Journal of Hydraulic Engineering*, **131**, 12, 1062–1073, 2005.
46. C.M. GARCÍA, P. JACKSON, M.H. GARCÍA, *Confidence intervals in the determination of turbulence parameter*, *Experiments in Fluids*, **40**, 4, 514–522, 2006.
47. D. POLITIS, H. WHITE, *Automatic block-length selection for the dependant bootstrap*, *Econometric Reviews*, **23**, 53–70, 2004.
48. G. CONSOLINI, P.D.E. MICHELIS, *Local intermittency measure analysis of AE index: The directly driven and unloading component*, *Geophysical Research Letters*, **32**, 5, 2005.

Received August 23, 2017; revised version December 30, 2017.

---